Dzyaloshinskii-Moriya interaction and magnetic skyrmions induced by curvature

Yonglong Ga,[1,2] Qirui Cui,[1] Jinghua Liang ⬡,[1] Dongxing Yu,[1] Yingmei Zhu,[1] Liming Wang,[1] and Hongxin Yang ⬡[1,2,*]

[1]*Ningbo Institute of Materials Technology and Engineering, Chinese Academy of Sciences, Ningbo 315201, China*
[2]*Center of Materials Science and Optoelectronics Engineering, University of Chinese Academy of Sciences, Beijing 100049, China*

Realizing sizable Dzyaloshinskii-Moriya interaction (DMI) in intrinsic two-dimensional (2D) magnets without any manipulation will greatly enrich potential application of spintronics devices. The simplest and most desirable situation should be 2D magnets with intrinsic DMI and intrinsic chiral spin textures. Here, we propose to realize DMI by designing periodic ripple structures with different curvatures in low-dimensional magnets and demonstrate the concept in both one-dimensional $CrBr_2$ and 2D $MnSe_2$ magnets by using first-principles calculations. We find that DMIs in curved $CrBr_2$ and $MnSe_2$ can be efficiently controlled by varying the curvature c, where c is defined as the ratio between the height h and the length l of the curved structure. Moreover, we unveil that the dependence of first-principles calculated DMI on curvature c can be well described by the three-site Fert-Lévy model. At last, we uncover that field-free magnetic skyrmions can be realized in curved $MnSe_2$ by using atomistic spin model simulations based on first-principles calculated magnetic parameters. The work will open an avenue for inducing DMI and chiral spin textures in simple 2D magnets via curvature.

I. INTRODUCTION

The antisymmetric exchange coupling, Dzyaloshinskii-Moriya interaction (DMI) [1,2], arising from inversion symmetry breaking and spin-orbit coupling (SOC), plays an essential role in stabilizing topological protected noncollinear chiral magnetic configurations [3–7]. The presence of DMI is confirmed in the noncentrosymmetric B20 material MnSi [8], in which magnetic skyrmions are first observed. Recently, many reports have further demonstrated DMI can be induced at interfaces of $3d/5d$ metal [9–11], metal/oxides [12–15], or light elements such as graphene [16,17], oxygen, hydrogen, etc. [18,19]. Notably, experimental progresses have demonstrated that magnetic order of two-dimensional (2D) magnets can persist down to monolayer, which is useful for the study of fundamental physics and for engineering spintronic devices [20–22]. As for noncollinear magnetism, several effective methods are proposed to obtain sizable DMI in 2D materials, such as in 2D Janus magnets [23–25], intrinsic 2D multiferroics [26,27], van der Waals ferromagnet-based heterostructures, etc. [28–32], in which inversion symmetry breaking plays a significant role.

In practice, it is inevitable to induce ripples for a 2D material either freestanding or on a substrate as long as the size of 2D material is large enough, which has been reported in graphene [33,34] and MoS_2 [35,36], etc. If such a curved system is magnetic, it is highly possible to achieve DMI in pure 2D magnets. Here, we propose to realize sizable DMI by designing periodic ripple structures with different curvatures in low-dimensional magnets. We demonstrate the concept in both one-dimensional (1D) $CrBr_2$ and 2D

$MnSe_2$ structures, in which DMI can be efficiently tuned by magnitude of curvatures. Moreover, we validate that the variation of curvature-dependent DMI can be well interpreted by Fert-Lévy mechanism. Interestingly, using atomistic spin model simulations based on first-principles calculated magnetic parameters, we find that field-free chiral magnetic skyrmions can be realized in 2D $MnSe_2$. These examples provide a routine towards realizing chiral magnetic skyrmions in 2D magnets with long-range magnetic orderings, e.g., $CrGeTe_2$ [37], CrI_3 [38], Fe_3GeTe_2 [39], etc.

II. COMPUTATIONAL DETAILS

Our first-principles calculations are performed within the framework of density-functional theory as implemented in the Vienna *Ab initio* Simulation Package (VASP) [40]. We choose the Perdew-Burke-Ernzerhof functionals of generalized gradient approximation (GGA) [41] to deal with the exchange-correlation energy. Besides, projector-augmented plane-wave method [42,43] is adopted to deal with the interaction between nuclear electrons and valence electrons. In order to correctly describe the $3d$ electrons, we employ the GGA + U method [44] with an effective $U = 2$ eV and $U = 3$ eV for Mn and Cr as reported in previous studies [45,46], respectively. We build up a $7 \times 1 \times 1$ $CrBr_2$ and $6\sqrt{3} \times 1 \times 1$ $MnSe_2$ supercells to construct magnetic structures with different curvatures. The energy cutoff for plane-wave expansion is set to 520 eV. Γ-centered $7 \times 1 \times 1$ for 1D $CrBr_2$ and $2 \times 18 \times 1$ for 2D $MnSe_2$ k-point meshes are adopted for the Brillouin-zone (BZ) integration to relax supercell, respectively. All the structures are fully relaxed until the Hellmann-Feynman force acting on each atom and convergence criteria for energy are 0.001 eV/Å and is 1×10^{-7} eV, respectively.
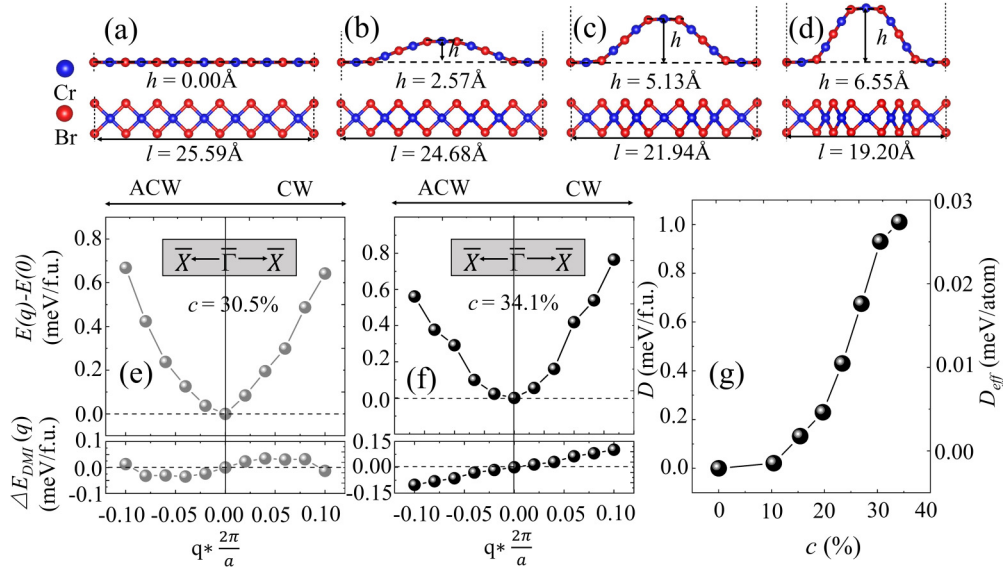
*hongxin.yang@nimte.ac.cn

FIG. 1. DMI of curved 1D $CrBr_2$. (a)–(d) Side (upper panel) and top (lower panel) views of 1D $CrBr_2$ with $c = 0.0\%$, $c = 10.4\%$, $c = 23.4\%$, and $c = 34.1\%$, respectively. Here, c is defined as the ratio between the height h and the length l of curved structure. (e), (f) Spin-spiral dispersion energy $E(q)$ (upper location) and DMI energy $\Delta E_{DMI}(q)$ (lower location) calculated as a function of spin-spiral vector q for $c = 30.5\%$ and $c = 34.1\%$, respectively. $E(0)$ represents the energy at $q = 0$. (g) Calculated total DMI D per supercell and effective DMI D_{eff} per magnetic atom as a function of curvature c.

III. ONE-DIMENSIONAL $CrBr_2$

For simplification of analysis, we first investigate curvature-dependent DMI in 1D magnet $CrBr_2$. Similar to $CuCl_2$ and $CuBr_2$, bulk $CrBr_2$ has the monoclinic space group $C12/m1$ [47–49]. In each $CrBr_2$ layer, the ribbons are made up of edge-sharing $CrBr_4$ squares along the b axis. It has been not experimentally reported whether one-dimensional $CrBr_2$ can be exfoliated from bulk so far. In our paper, we use the simple 1D structure to demonstrate the dependence of DMI on curvature c. The obtained 1D $CrBr_2$ has D_{2h} crystal symmetry which preserved spatial inversion symmetry, as shown in Fig. 1(a). For achieving ripples, a $7 \times 1 \times 1$ supercell is constructed and the length l of the entire supercell is adjusted gradually in our calculations. Next, we keep two unit cells (located at the edges of the supercell) fixed

in the z direction and relax all other atoms to obtain final curved structures [Figs. 1(b)–1(d)]. In order to articulate our ideas, we present the schematic diagram (Fig. 2) consisting of sine and piecewise functions, in which the inversion symmetry with symmetry center i of sine function (red dotted line) will be broken in the piecewise function (blue line). This piecewise structure is an approximation for the effect of substrate on curvature. With this premise, we study how magnetic parameters change under different curvature c for a series of curved structures [Figs. 1(a)–1(d)]. Firstly, we study curvature-dependent magnetic properties of 1D $CrBr_2$. Figure 3(a) shows the ferromagnetic (FM) and antiferromagnetic (AFM) configurations. It is found that the calculated energy difference between AFM and FM evidently decreases with increasing c, as shown in Fig. 3(c). Moreover, the spin ordering tends to be AFM when c is larger than 15.4%. In
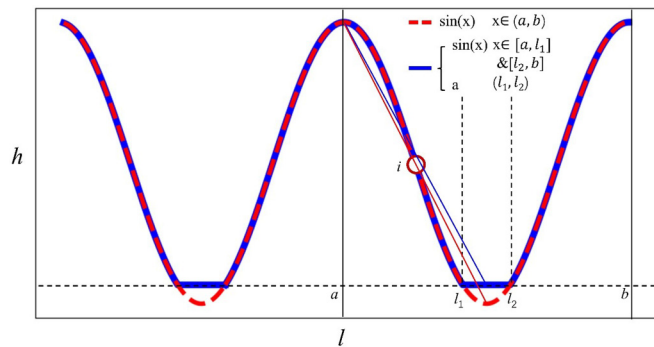

FIG. 2. Schematic diagram consisting of sine function (red dotted line) and piecewise function (blue line). The inversion symmetry with symmetry center i of sine function will be broken in the piecewise function.
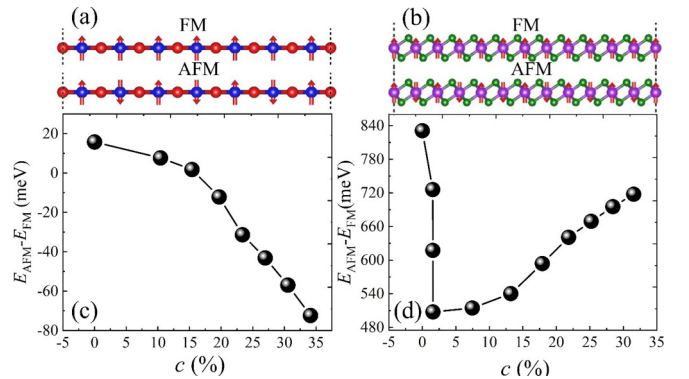

FIG. 3. (a), (b) FM and AFM spin configurations of $CrBr_2$ and $MnSe_2$, respectively. (c), (d) Energy differences between AFM and FM for $CrBr_2$ and $MnSe_2$ under different curvature c, respectively.
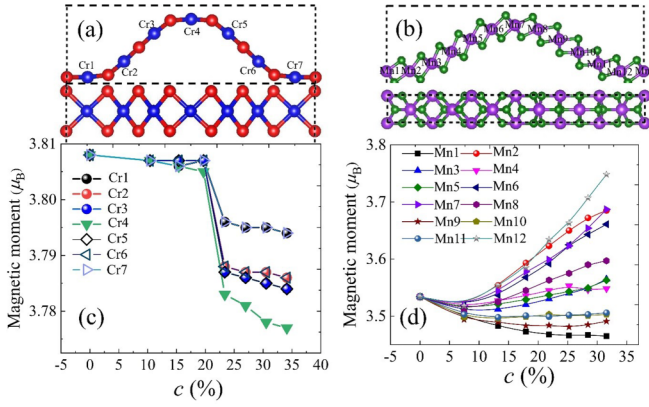
FIG. 4. (a), (b) Curved 1D $CrBr_2$ and 2D $MnSe_2$ structures, respectively. (c), (d) Representation of the absolute value of magnetic moment per Cr and Mn atom as c increases, respectively.

Fig. 4(a), we also investigate absolute value of magnetic moment per Cr atoms as c increases. In general, the magnetic moment variation of each magnetic atom is relatively weak and tends to decrease with increase of curvature.

Figure 1(g) shows the result of DMI for curved 1D $CrBr_2$ with different c. Obviously, DMI is strongly dependent on curvature c and the calculated DMI strength increases with the increment of curvature c. Here, a positive D represents spin configuration of anticlockwise chirality, and a negative one represents clockwise (CW) chirality. For total DMI D of

1D $CrBr_2$ with different curvature c, its value varies from 0 to 1.0 meV/f.u. (formula unit). Otherwise, in Figs. 1(e) and 1(f) the total energy $E(q)$ and DMI energy $\Delta E_{DMI}(q)$ including SOC are presented as a function of spin-spiral vector q along the $\bar{\Gamma} - \bar{X}$ direction in 2D BZ for $c = 30.5\%$ and $c = 34.1\%$, respectively. The extracted DMI are found to be 0.93 and 1.00 meV/f.u., respectively, suggesting that DMI of 1D $CrBr_2$ is directly associated with the existence of curvature. Considering the fact that 2D magnets, such as $CrGeTe_3$, CrI_3, Fe_3GeTe_2, and $MnSe_2$ [50] with long-range ferromagnetic orderings have been synthesized experimentally, we take the simplest one, $MnSe_2$, as an example to further investigate the feasibility of tunable DMI in 2D magnets.

IV. TWO-DIMENSIONAL $MnSe_2$

It was recently reported that monolayer 2D $MnSe_2$ with D_{3d} crystal symmetry is a room-temperature ferromagnet [50]. The optimized $MnSe_2$ structure is presented in Fig. 5(a). It can be seen that each Mn atom is surrounded by six non-magnetic Se atoms that make up an octahedron. Similar to 1D $CrBr_2$, we construct a $6\sqrt{3} \times 1 \times 1$ supercell to obtain ripple structures, in which Mn atoms of three unit cells (located at initial and terminal of the supercell) are fixed in the z direction and the other atoms are relaxed [Figs. 5(b)–5(d)]. To understand magnetism associated with curved structures, we construct FM and AFM states in Fig. 3(b). It is found that the energy difference between AFM and FM suddenly decreases and then keeps increasing as the c gradually increases
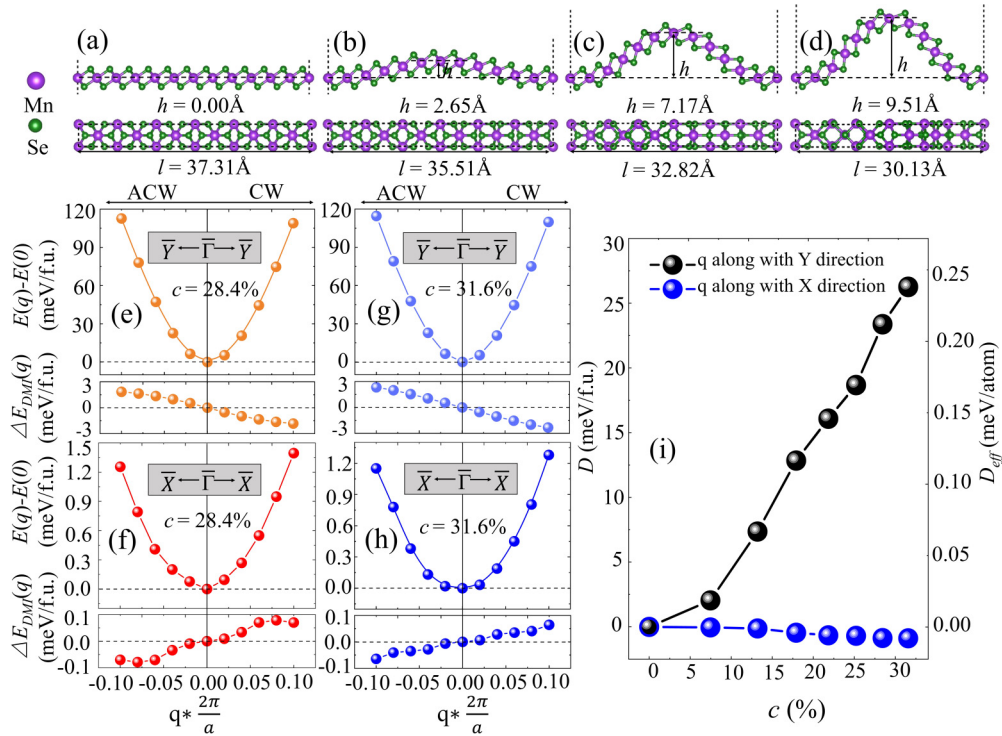

FIG. 5. DMI of curved 2D $MnSe_2$. (a)–(d) Side (upper panel) and top (lower panel) views of 2D $MnSe_2$ with $c = 0.0\%$, $c = 7.5\%$, $c = 21.8\%$, and $c = 31.6\%$, respectively. Here, c is defined as the ratio between the height h and the length l of curved structure. (e)–(h) Spin-spiral dispersion energy $E(q)$ (upper location) and DMI energy $\Delta E_{DMI}(q)$ (lower location) calculated as a function of spin-spiral vector q for $c = 28.4\%$ and $c = 31.6\%$, respectively. $E(0)$ represents the energy at $q = 0$. (i) Calculated total DMI D per supercell and effective DMI D_{eff} per magnetic atom as a function of curvature c.

[Fig. 3(d)]. We also compute the magnetic moment of Mn atoms from Mn1 to Mn12, as shown in Fig. 4(d). Compared to 1D CrBr$_2$, there is a distinct difference that the magnetic moments of Mn atoms located at peaks and troughs have large variation due to the locally severe structural deformation, while others do not change much.

In Fig. 5(i), we display the calculated results of DMI for 2D MnSe$_2$ with curvature. In 2D MnSe$_2$ structure, the global tendency of DMI is increasing as c gradually increases, similar to that of 1D CrBr$_2$. In 2D MnSe$_2$, there are two DMI vectors when spin-spiral vector q propagates along directions of $\bar{\Gamma} - \bar{X}$ and $\bar{\Gamma} - \bar{Y}$ in the 2D BZ, in which the calculated values are in the range of 0–0.88 meV/f.u. and 0–26.29 meV/f.u., respectively. Obviously, compared to that $\bar{\Gamma} - \bar{Y}$ direction, the DMI strength along with $\bar{\Gamma} - \bar{X}$ direction is almost negligible. Thus, we focus on the DMI vector in the $\bar{\Gamma} - \bar{Y}$ direction below. The energy dispersion $E(q)$ and the DMI energy $\Delta E_{\text{DMI}}(q)$ associated with spin-spiral vector q for $c = 28.4\%$ and $c = 31.6\%$ are shown in Figs. 5(e)–5(h). The extracted DMI parameters D by taking the slope of dispersion in the vicinity of ground state are 23.4 and 26.3 meV/f.u., respectively. For convenience in comparison, we also convert the total DMI per supercell to per magnetic atom as the effective DMI D_{eff} [Fig. 1(g) and Fig. 5(i)]. The D_{eff}, 0.21 and 0.24 meV/atom in 2D MnSe$_2$ induced by curvature with $c = 28.4\%$ and $c = 31.6\%$, which are comparable to those of Co/Ru(0001) [51] or Co/graphene interfaces [16,17], are highly possible to stabilize magnetic chiral spin textures in 2D magnets with long-range magnetic orderings.

V. DISCUSSION

To further understand the variation of curvature-induced DMI above, the DMI effect of curved structure can be modeled as the sum of each M-X-M trimer, where M and X represent the magnetic and nonmagnetic atoms, respectively. Based on three-site Fert-Lévy model [52], the hopping of spins between two magnetic atoms (i and j) can induce DMI through a nonmagnetic atom (l) with SOC. The theoretical formulism of antisymmetric DMI can be expressed as

$$\vec{D}_{ijl}(\vec{R}_{li}\vec{R}_{lj}\vec{R}_{ij}) = -V_{\text{SOC}} \frac{(\vec{R}_{li} \cdot \vec{R}_{lj})(\vec{R}_{li} \times \vec{R}_{lj})}{|\vec{R}_{li}|^3 |\vec{R}_{lj}|^3 |\vec{R}_{ij}|}, \quad (1)$$

where $\vec{R}_{li}$, $\vec{R}_{lj}$, and $\vec{R}_{ij}$ are the corresponding distance vectors between atoms in the three-site model. V_{SOC} is a SOC-governed material parameter; its expressions can be written as $[(135\pi)/32][(\lambda_d \Gamma^2)/(k_F^3 E_F^2)]\sin(Z_d \pi/10)$, in which λ_d, k_F, E_F, and Z_d are the SOC constant, Fermi vector, Fermi energy, and the number of d electrons, respectively. Γ is the interaction parameter between the localized spins and the spins of conduction electrons. In a curved magnet, the total DMI can be obtained by summing over all M-X-M trimers and we can further simplify the above Eq. (1) as

$$\vec{D} = -V_{\text{SOC}} \sum_{i=1}^{n} \frac{2\sin(2\theta_i)\sin^2\left(\frac{1}{2}\theta_i\right)}{a_i^3}, \quad (2)$$

where i is the index of summation, and θ_i and a_i represent bond angle of each M-X-M trimer and bond length between
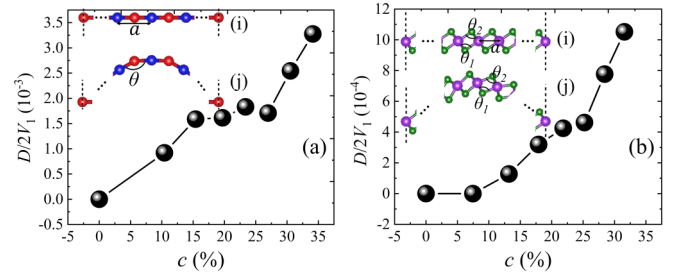

FIG. 6. Summing over all M-X-M trimers based on Fert-Lévy model [Eq. (3)] in (a) 1D CrBr$_2$ and (b) 2D MnSe$_2$, respectively. Insets (i) and (j) represent structures with/without inversion symmetry, in which both θ (θ_i, $i = 1, 2$) and a are bond angle of each M-X-M trimer and bond length between the nearest-neighbor M atoms.

the nearest-neighbor M atoms in whole curved structure, respectively. In order to describe curvature dependence of DMI in Fert-Lévy model, we assume that V_{SOC} is a constant for a given system. Then we can provide a quantitative understanding for curvature-induced DMI based on Eq. (2). Insets i in Figs. 6(a) and 6(b) present the schematic structures with inversion symmetry, which will lead to the offset of total DMI. However, the inversion symmetry breaking arising from curvature will induce an uncompensated DMI in the noncentrosymmetric three-site interaction [insets j in Figs. 6(a) and 6(b)]. For 1D CrBr$_2$, in order to build up the relationship between curvature and DMI, the calculated θ_i and a_i of each Cr-Br-Cr trimer are brought into Eq. (2). The result shows that $D/2V_{\text{SOC}}$ increases with increasing curvature c, as is shown in Fig. 6(a). Similar to that of 1D CrBr$_2$, we can determine the θ_i and a_i of each Mn-Se-Mn trimer in curved 2D MnSe$_2$ and one can see that $D/2V_{\text{SOC}}$ increases as curvature c increases when θ_i and a_i are brought into Eq. (2) as shown in Fig. 6(b). These results are in line with given results from first-principles calculations. More interestingly, notice that the whole curve structure is composed of several similar M-X-M trimers in our studied system, and we find that θ_i and a_i of each M-X-M trimer present a small tendency of change as a whole in curved structure with increasing curvature c. Therefore, we propose a simple model, in which average bond angle $\bar{\theta}$ of Cr-Br-Cr (Mn-Se-Mn) triples and average bond length $\bar{a}$ of the nearest-neighbor Cr (Mn) atoms in whole curve magnet are described as key parameters to further examine the relationship between curvature and DMI. We plot the dependences of $\bar{\theta}$ and $\bar{a}$ with respect to curvature c as shown in Figs. 7(a) and 7(b). We can
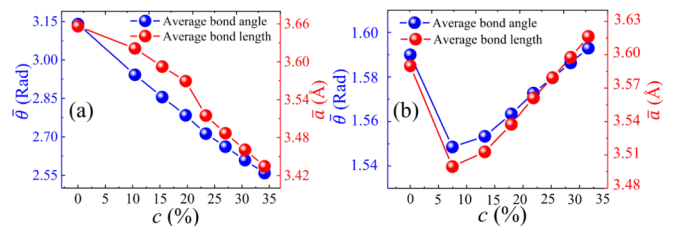

FIG. 7. Calculated average bond angle $\bar{\theta}$ and average bond length $\bar{a}$ as a function of curvature c for (a) 1D CrBr$_2$ and (b) 2D MnSe$_2$.
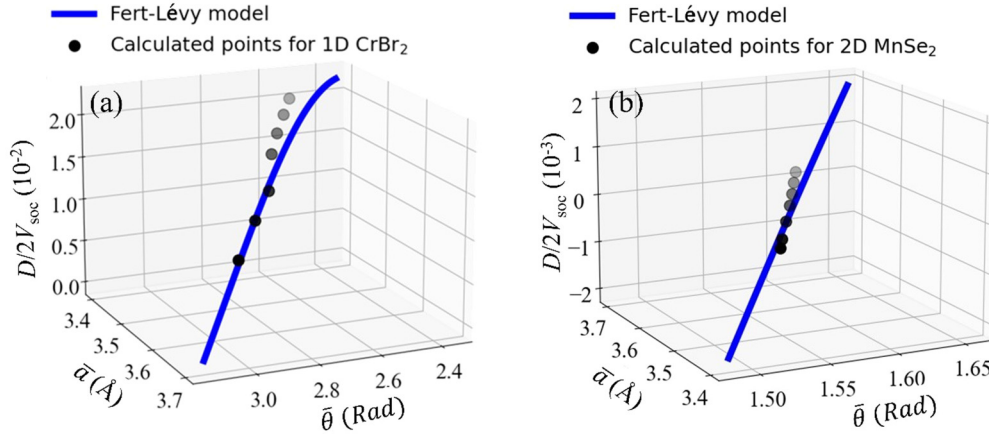
FIG. 8. Plotted theoretical curve and calculated results by using Fert-Lévy model [Eq. (2)]. (a) and (b) indicate the $D/2V_{SOC}$ as a function of average bond angle $\bar{\theta}$ and average bond length $\bar{a}$ in 1D CrBr$_2$ and 2D MnSe$_2$, respectively.

further simplify Eq. (2) as

$$\bar{D} = -V_{SOC}\frac{2\sin(2\bar{\theta})\sin^2\left(\frac{1}{2}\bar{\theta}\right)}{\bar{a}^3}. \qquad (3)$$

Overall, one can see that $D/2V_{SOC}$ increases for both 1D CrBr$_2$ and 2D MnSe$_2$ with increasing curvature c when $\bar{\theta}$ and $\bar{a}$ are brought into Eq. (3), as shown in Figs. 8(a) and 8(b). This is also consistent with given results from first-principles calculations. Thus, our findings based on both first-principles calculations and Fert-Lévy model demonstrate that curvature is an effective way to realize DMI in 1D CrBr$_2$ and 2D MnSe$_2$.

VI. REALIZATION OF SKYRMIONS IN 2D MnSe$_2$

To explore the formation of such chiral spin textures in curved 2D MnSe$_2$, we apply atomistic spin model simulations [53] for the magnetization dynamics simulation based on magnetic parameters with curvature c of 31.6% from first-principles calculations. To obtain final spin configurations, the atomistic Landau-Lifshitz-Gilbert equation is given:

$$\frac{\partial S_i}{\partial t} = -\frac{\gamma}{(1+\lambda^2)}\left[S_i \times H_{eff}^i + \lambda S_i \times \left(S_i \times H_{eff}^i\right)\right]. \qquad (4)$$

Here γ is the gyromagnetic ratio, λ is the Gilbert damping constant, and S_i is the unit vector, which is defined as $\frac{\mu_i}{|\mu_i|}$, where μ_i represents the magnetic moment of the ith magnetic atom. H_{eff}^i is the effective magnetic field on each S_i and can be obtained by the following equation: $H_{eff}^i = -\frac{1}{\mu_i}\frac{\partial H}{\partial S_i}$, in which H represents the total spin Hamiltonian. In simulations, we set a 60-nm-width square with periodic boundary condition from an initial random state to obtain final spin textures. These parameters, including effective exchange constant J_{eff}, effective DMI parameter D_{eff}, magnetic anisotropy K, dipole-dipole interaction K_{dip} and magnetic moment of Mn atoms, are 14.94 meV, 0.24 meV, 0.17 meV, −0.176 meV, and 3.58 μ_B, respectively, and the methods to calculate J_{eff}, K, D_{eff}, and K_{dip} are described in the Appendix. In addition, we apply the theoretical formula $\bar{R} = \pi D\sqrt{\frac{A}{16AK^2 - \pi^2 D^2 K}}$ [54] to predict the radius $\bar{R}$ of skyrmion, which is close to 20 nm. We can find that the size of chiral structure is much larger than

the ripple wavelength. Thus, we used the flat crystal structure to simulate our chiral magnetic structures in the atomic magnetic simulations. In simulations, Fig. 9 shows the spin textures of curved MnSe$_2$ in $c = 31.6\%$. Interestingly, magnetic skyrmion spin texture with diameter of around 20 nm emerges under zero magnetic field as shown in Figs. 9(a) and 9(b). The calculated topological charge Q is −1 for skyrmion by using the formula $Q = \frac{1}{4\pi}\int S \cdot (\partial_x S \times \partial_y S)dxdy$, where S represents the unit vector; x and y are the coordinates.

VII. CONCLUSION

In summary, we obtain sizable DMI in both 1D CrBr$_2$ and 2D MnSe$_2$ by using ripple structures with different curvatures via using first-principles calculations. We unveil that quite large DMI can be induced in curved structure, in which breaking of spatial inversion plays an important role. In addition, with the help of three-site Fert-Lévy model, the DMI dependence on the magnitude of curvature is successfully interpreted. Via atomistic spin model simulations, we further uncover that magnetic skyrmions can be induced without external field in curved 2D MnSe$_2$. Considering the experimental progress in 2D magnets, such as CrGeTe$_3$, CrI$_3$ and Fe$_3$GeTe$_2$, etc., our results open up opportunities for development of spintronics.

Note added. We recently became aware that Edström *et al.* also predicted that a cycloidal state can be stabilized by an
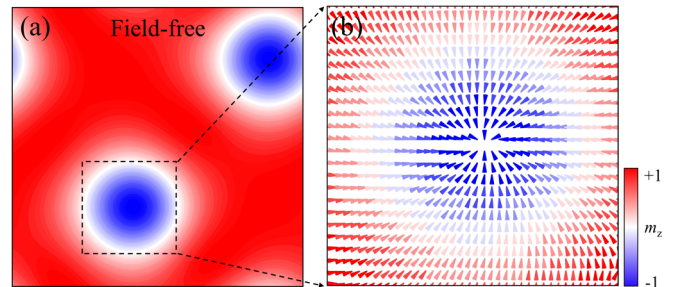

FIG. 9. (a) Atomistic spin model simulated spin configurations for a curved MnSe$_2$ with curvature c of 31.6%; (b) zoom in of an isolated skyrmion profile.

effective curvature-induced DMI in curved nanotube of CrI_3 [55].

APPENDIX: CALCULATIONS OF MAGNETIC PARAMETERS

1. Dzyaloshinskii-Moriya interaction D

Dzyaloshinskii-Moriya interaction (DMI) is beneficial to form the noncollinear magnetic textures, in which the neighboring spins tend to align perpendicular to each other. The energy term can be described as

$$E_{DM} = \sum_{i,j} \boldsymbol{D}_{ij} \cdot (\boldsymbol{S}_i \times \boldsymbol{S}_j), \qquad (A1)$$

where $\boldsymbol{D}_{ij}$ represents the DMI vector; $\boldsymbol{S}_i$ and $\boldsymbol{S}_j$ are the spins of nearest-neighbor magnetic atoms. We adopt the qSO method based on generalized Bloch theorem and treat SOC within the first-order perturbation theory [26,56,57], in which the total energy $E(\boldsymbol{q})$ as the function of spin-spiral vector $\boldsymbol{q}$ is calculated along the high-symmetry direction of $\bar{\Gamma} - \bar{X}$ and $\bar{\Gamma} - \bar{Y}$ in our studied system. To extract the DMI parameter, a Γ-centered $7 \times 1 \times 1$ for 1D $CrBr_2$ and $2 \times 18 \times 1$ k mesh for 2D $MnSe_2$ are considered to compute the spin-spiral energy $E(\boldsymbol{q})$ in the interval of q from $-0.1\frac{2\pi}{a}$ to $0.1\frac{2\pi}{a}$ in a self-consistent way. The nonlinear spin-spiral structure $\boldsymbol{m} = [\sin(\boldsymbol{q} \cdot \boldsymbol{r}_i), 0, \cos(\boldsymbol{q} \cdot \boldsymbol{r}_i)]$ rotates along the axis of spin spiral parallel to the y axis, where $\boldsymbol{q}$ represents the spin-spiral vector and $\boldsymbol{r}_i$ is the location of the ith atom. (When the rotation axis is x axis, the nonlinear spin-spiral structure $\boldsymbol{m} = [0, \sin(\boldsymbol{q} \cdot \boldsymbol{r}_i), \cos(\boldsymbol{q} \cdot \boldsymbol{r}_i)]$. Then, DMI energy can be written as

$$E_{DMI}(\boldsymbol{q}) = \sum_{i,j} \boldsymbol{D}_y \sin(\boldsymbol{q} \cdot \boldsymbol{r}_{ij}), \qquad (A2)$$

where $\boldsymbol{D}_y$ represents the DM vector perpendicular to the propagation direction of spin spirals, and $\boldsymbol{r}_{ij}$ is the unit vector between sites i and j. Finally, the DMI parameter can be obtained by taking the slope of $\Delta E_{DMI}(\boldsymbol{q})$ with respect to spin-spiral vector $\boldsymbol{q}$, where $\Delta E_{DMI}(\boldsymbol{q})$ is the energy difference between $E(\boldsymbol{q})$ and $E(-\boldsymbol{q})$. Furthermore, the final form of DMI energy can be simplified as

$$\Delta E_{DMI}(\boldsymbol{q}) = E(\boldsymbol{q}) - E(-\boldsymbol{q}) = 2 \sum_{i,j} \boldsymbol{D}_y \sin(\boldsymbol{q} \cdot \boldsymbol{r}_{ij}). \qquad (A3)$$

For small $\boldsymbol{q} = (q, 0, 0)$ vector, we have the relationships

$$\Delta E_{DM}(\boldsymbol{q}) = 2q \sum_{i,j} D_{y0} r_{ij,x} = Dq, \qquad (A4)$$

where

$$D = 2 \sum_{i,j} D_{y0} r_{ij,x}. \qquad (A5)$$

Here, the direction of DM vector depends on the propagation direction of spin-spiral $\boldsymbol{q}$ of the whole Brillouin zone.

2. Effective DMI value D_{eff}

In our calculations, we convert the total DMI D per supercell to per magnetic atom as the effective D_{eff}. For 1D $CrBr_2$, $D = 14\pi D_{eff}$. For 2D $MnSe_2$, $D = 36\pi D_{eff}$.

3. Magnetocrystalline anisotropy energy K

K is defined as the energy difference between in-plane (100) and out-of-plane (001) magnetized axis:

$$K = E_{100} - E_{001} \qquad (A6)$$

4. Effective exchange coupling constant J_{eff}

As is shown in Fig. 3(b), we set different magnetic configurations FM and AFM for $MnSe_2$. We consider the Heisenberg model on a hexagonal lattice,

$$H = \sum_{ij} J_{eff} \vec{S}_i \cdot \vec{S}_j. \qquad (A7)$$

Then, effective exchange-coupling constant can be solved by the following formula:

$$E_{FM} = -\frac{1}{2} 12(6J_{eff}) + E_{other}, \qquad (A8)$$

$$E_{AFM} = -\frac{1}{2} 12(-2J_{eff}) + E_{other}, \qquad (A9)$$

$$J_{eff} = \frac{E_{AFM} - E_{FM}}{48}, \qquad (A10)$$

where the positive or negative value corresponds to FM or AFM coupling.

5. Dipole-dipole contribution to K_{dip}

The dipole-dipole interaction contribution to K is the sum of all magnetostatic dipole-dipole interactions up to infinity [58,59] and is calculated by following formula:

$$E_{dip} = -\frac{1}{2} \left\{ \frac{\mu_0}{4\pi V_{u.c.}} \right\} \sum_{i,j=1}^{N} \frac{(\boldsymbol{m}_i \cdot \boldsymbol{m}_j) r_{ij}^2 - 3(\boldsymbol{m}_i \cdot \boldsymbol{r}_{ij})(\boldsymbol{m}_j \cdot \boldsymbol{r}_{ij})}{r_{ij}^5}, \qquad (A11)$$

where $\boldsymbol{m}_i$ and $\boldsymbol{m}_j$ represent the unit vector of magnetization at position $\boldsymbol{r}_i$ and $\boldsymbol{r}_j$; $\boldsymbol{r}_{ij}$ is the unit vector between site i and j. In calculations, we choose a $150 \times 150 \times 1$ supercell to obtain the dipole-dipole interaction between two magnetic atoms in 2D $MnSe_2$.

[1] I. Dzyaloshinsky, A thermodynamic theory of "weak" ferromagnetism of antiferromagnetics, J. Chem. Phys. Solids **4**, 241 (1958).

[2] T. Moriya, Anisotropic superexchange interaction and weak ferromagnetism, Phys. Rev. **120**, 91 (1960).

[3] A. Thiaville, S. Rohart, É. Jué, V. Cros, and A. Fert, Dynamics of Dzyaloshinskii domain walls in ultrathin magnetic films, Europhys. Lett. **100**, 57002 (2012).

[4] B. Göbel, A. Mook, J. Henk, I. Mertig, and O. A. Tretiakov, Magnetic bimerons as skyrmion analogues in in-plane magnets, Phys. Rev. B **99**, 060407(R) (2019).

[5] H. Jani, J. C. Lin, J. Chen, J. Harrison, F. Maccherozzi, J. Schad, S. Prakash, C. B. Eom, A. Ariando, T. Venkatesan, and P. G. Radaelli, Antiferromagnetic half-skyrmions and bimerons at room temperature, Nature (London) **590**, 74 (2021).

[6] A. N. Bogdanov and D. A. Yablonsky, Thermodynamically stable "vortices" in magnetically ordered crystals. The mixed state of magnets, Sov. Phys. JETP **68**, 101 (1989).

[7] X. Z. Yu, N. Kanazawa, Y. Onose, K. Kimoto, W. Z. Zhang, S. Ishiwata, Y. Matsui, and Y. Tokura, Near room-temperature formation of a skyrmion crystal in thin-films of the helimagnet FeGe, Nat. Mater. **10**, 106 (2011).

[8] S. Mühlbauer, B. Binz, F. Jonietz, C. Pfleiderer, A. Rosch, A. Neubauer, R. Georgii, and P. Böni, Skyrmion lattice in a chiral magnet, Science **323**, 915 (2009).

[9] S. Heinze, K. von Bergmann, M. Menzel, J. Brede, A. Kubetzka, R. Wiesendanger, G. Bihlmayer, and S. Blügel, Spontaneous atomic-scale magnetic skyrmion lattice in two dimensions, Nat. Phys. **7**, 713 (2011).

[10] O. Boulle, J. Vogel, H. Yang, S. Pizzini, D. de Souza Chaves, A. Locatelli, T. O. Mentes, A. Sala, L. D. Buda-Prejbeanu, O. Klein, M. Belmeguenai, Y. Roussigne, A. Stashkevich, S. M. Cherif, L. Aballe, M. Foerster, M. Chshiev, S. Auffret, I. M. Miron, and G. Gaudin, Room-temperature chiral magnetic skyrmions in ultrathin magnetic nanostructures, Nat. Nanotechnol. **11**, 449 (2016).

[11] W. Jiang, P. Upadhyaya, W. Zhang, G. Yu, M. B. Jungfleisch, F. Y. Fradin, J. E. Pearson, Y. Tserkovnyak, K. L. Wang, O. Heinonen, S. G. E. t. Velthuis, and A. Hoffmann, Blowing magnetic skyrmion bubbles, Science **349**, 283 (2015).

[12] M. Schott, A. Bernand-Mantel, L. Ranno, S. Pizzini, J. Vogel, H. Bea, C. Baraduc, S. Auffret, G. Gaudin, and D. Givord, The skyrmion switch: Turning magnetic skyrmion bubbles on and off with an electric field, Nano Lett. **17**, 3006 (2017).

[13] H. Yang, O. Boulle, V. Cros, A. Fert, and M. Chshiev, Controlling Dzyaloshinskii-Moriya interaction via chirality dependent atomic-layer stacking, insulator capping and electric field, Sci. Rep. **8**, 12356 (2018).

[14] D. d. S. Chaves, F. Ajejas, V. Křižáková, J. Vogel, and S. Pizzini, Oxidation dependence of the Dzyaloshinskii-Moriya interaction in Pt/Co/MOx trilayers (M = Al or Gd), Phys. Rev. B **99**, 144404 (2019).

[15] H. T. Nembach, E. Jué, E. R. Evarts, and J. M. Shaw, Correlation between Dzyaloshinskii-Moriya interaction and orbital angular momentum at an oxide-ferromagnet interface, Phys. Rev. B **101**, 020409(R) (2020).

[16] H. Yang, G. Chen, A. A. C. Cotta, A. T. N'Diaye, S. A. Nikolaev, E. A. Soares, W. A. A. Macedo, K. Liu, A. K. Schmid, A. Fert, and M. Chshiev, Significant Dzyaloshinskii-Moriya interaction at graphene-ferromagnet interfaces due to the Rashba effect, Nat. Mater. **17**, 605 (2018).

[17] F. Ajejas, A. Gudin, R. Guerrero, A. Anadon Barcelona, J. M. Diez, L. de Melo Costa, P. Olleros, M. A. Nino, S. Pizzini, J. Vogel, M. Valvidares, P. Gargiani, M. Cabero, M. Varela, J. Camarero, R. Miranda, and P. Perna, Unraveling Dzyaloshinskii-Moriya interaction and chiral nature of graphene/cobalt interface, Nano Lett. **18**, 5364 (2018).

[18] G. Chen, A. Mascaraque, H. Jia, B. Zimmermann, M. Robertson, R. L. Conte, M. Hoffmann, M. A. G. Barrio, H. Ding, R. Wiesendanger, E. G. Michel, S. Blügel, A. K. Schmid, and K. Liu, Large Dzyaloshinskii-Moriya interaction induced by chemisorbed oxygen on a ferromagnet surface, Sci. Adv. **6**, eaba4924 (2020).

[19] G. Chen, M. Robertson, M. Hoffmann, C. Ophus, A. L. Fernandes Cauduro, R. Lo Conte, H. Ding, R. Wiesendanger, S. Blügel, A. K. Schmid, and K. Liu, Observation of Hydrogen-Induced Dzyaloshinskii-Moriya Interaction and Reversible Switching of Magnetic Chirality, Phys. Rev. X **11**, 021015 (2021).

[20] D. Zhong, K. L. Seyler, X. Linpeng, R. Cheng, N. Sivadas, B. Huang, E. Schmidgall, T. Taniguchi, K. Watanabe, M. A. McGuire, W. Yao, D. Xiao, K.-M. C. Fu, and X. Xu, Van der Waals engineering of ferromagnetic semiconductor heterostructures for spin and valleytronics, Sci. Adv. **3**, e1603113 (2017).

[21] K. S. Burch, D. Mandrus, and J. G. Park, Magnetism in two-dimensional van der Waals materials, Nature (London) **563**, 47 (2018).

[22] M. Gibertini, M. Koperski, A. F. Morpurgo, and K. S. Novoselov, Magnetic 2D materials and heterostructures, Nat. Nanotechnol. **14**, 408 (2019).

[23] J. Liang, W. Wang, H. Du, A. Hallal, K. Garcia, M. Chshiev, A. Fert, and H. Yang, Very large Dzyaloshinskii-Moriya interaction in two-dimensional Janus manganese dichalcogenides and its application to realize skyrmion states, Phys. Rev. B **101**, 184401 (2020).

[24] C. Xu, J. Feng, S. Prokhorenko, Y. Nahas, H. Xiang, and L. Bellaiche, Topological spin texture in Janus monolayers of the chromium trihalides Cr(I, X)$_3$, Phys. Rev. B **101**, 060404(R) (2020).

[25] Q. Cui, J. Liang, Z. Shao, P. Cui, and H. Yang, Strain-tunable ferromagnetism and chiral spin textures in two-dimensional Janus chromium dichalcogenides, Phys. Rev. B **102**, 094425 (2020).

[26] J. Liang, Q. Cui, and H. Yang, Electrically switchable Rashba-type Dzyaloshinskii-Moriya interaction and skyrmion in two-dimensional magnetoelectric multiferroics, Phys. Rev. B **102**, 220409(R) (2020).

[27] C. Xu, P. Chen, H. Tan, Y. Yang, H. Xiang, and L. Bellaiche, Electric-Field Switching of Magnetic Topological Charge in Type-I Multiferroics, Phys. Rev. Lett. **125**, 037203 (2020).

[28] W. Sun, W. Wang, H. Li, G. Zhang, D. Chen, J. Wang, and Z. Cheng, Controlling bimerons as skyrmion analogues by ferroelectric polarization in 2D van der Waals multiferroic heterostructures, Nat. Commun. **11**, 5930 (2020).

[29] C.-K. Li, X.-P. Yao, and G. Chen, Writing and deleting skyrmions with electric fields in a multiferroic heterostructure, Phys. Rev. Research **3**, L012026 (2021).

[30] Y. Wu, S. Zhang, J. Zhang, W. Wang, Y. L. Zhu, J. Hu, G. Yin, K. Wong, C. Fang, C. Wan, X. Han, Q. Shao, T. Taniguchi,

K. Watanabe, J. Zang, Z. Mao, X. Zhang, and K. L. Wang, Neel-type skyrmion in WTe$_2$/Fe$_3$GeTe$_2$ van der Waals heterostructure, Nat. Commun. **11**, 3860 (2020).

[31] T.-E. Park, L. Peng, J. Liang, A. Hallal, F. S. Yasin, X. Zhang, K. M. Song, S. J. Kim, K. Kim, M. Weigand, G. Schütz, S. Finizio, J. Raabe, K. Garcia, J. Xia, Y. Zhou, M. Ezawa, X. Liu, J. Chang, H. C. Koo, Y. D. Kim, M. Chshiev, A. Fert, H. Yang, X. Yu, and S. Woo, Néel-type skyrmions and their current-induced motion in van der Waals ferromagnet-based heterostructures, Phys. Rev. B **103**, 104410 (2021).

[32] M. Yang, Q. Li, R. V. Chopdekar, R. Dhall, J. Turner, J. D. Carlström, C. Ophus, C. Klewe, P. Shafer, A. T. N'Diaye, J. W. Choi, G. Chen, Y. Z. Wu, C. Hwang, F. Wang, and Z. Q. Qiu, Creation of skyrmions in van der Waals ferromagnet Fe$_3$GeTe$_2$ on (Co/Pd)$_n$ superlattice, Sci. Adv. **6**, eabb5157 (2020).

[33] A. Fasolino, J. H. Los, and M. I. Katsnelson, Intrinsic ripples in graphene, Nat. Mater. **6**, 858 (2007).

[34] J. C. Meyer, A. K. Geim, M. I. Katsnelson, K. S. Novoselov, T. J. Booth, and S. Roth, The structure of suspended graphene sheets, Nature (London) **446**, 60 (2007).

[35] J. Brivio, D. T. Alexander, and A. Kis, Ripples and layers in ultrathin MoS$_2$ membranes, Nano Lett. **11**, 5148 (2011).

[36] P. Miro, M. Ghorbani-Asl, and T. Heine, Spontaneous ripple formation in Mos(2) Monolayers: Electronic structure and transport effects, Adv. Mater. **25**, 5473 (2013).

[37] C. Gong, L. Li, Z. Li, H. Ji, A. Stern, Y. Xia, T. Cao, W. Bao, C. Wang, Y. Wang, Z. Q. Qiu, R. J. Cava, S. G. Louie, J. Xia, and X. Zhang, Discovery of intrinsic ferromagnetism in two-dimensional van der Waals crystals, Nature (London) **546**, 265 (2017).

[38] B. Huang, G. Clark, E. Navarro-Moratalla, D. R. Klein, R. Cheng, K. L. Seyler, D. Zhong, E. Schmidgall, M. A. McGuire, D. H. Cobden, W. Yao, D. Xiao, P. Jarillo-Herrero, and X. Xu, Layer-dependent ferromagnetism in a van der Waals crystal down to the monolayer limit, Nature (London) **546**, 270 (2017).

[39] Z. Fei, B. Huang, P. Malinowski, W. Wang, T. Song, J. Sanchez, W. Yao, D. Xiao, X. Zhu, A. F. May, W. Wu, D. H. Cobden, J. H. Chu, and X. Xu, Two-dimensional itinerant ferromagnetism in atomically thin Fe$_3$GeTe$_2$, Nat. Mater. **17**, 778 (2018).

[40] G. Kresse and J. Furthmüller, Efficient iterative schemes for ab initio total-energy calculations using a plane-wave basis set, Phys. Rev. B **54**, 11169 (1996).

[41] J. P. Perdew, K. Burke, and M. Ernzerhof, Generalized Gradient Approximation Made Simple, Phys. Rev. Lett. **77**, 3865 (1996).

[42] G. Kresse and J. Hafner, *Ab initio* molecular dynamics for liquid metals, Phys. Rev. B **47**, 558 (1993).

[43] G. Kresse and J. Furthmüller, Efficiency of *ab-initio* total energy calculations for metals and semiconductors using a plane-wave basis set, Comput. Mater. Sci. **6**, 15 (1996).

[44] V. I. Anisimov, F. Aryasetiawan, and A. I. Lichtenstein, First-principles calculations of the electronic structure and spectra of strongly correlated systems: The LDA+U method, J. Phys.: Condens. Matter **9**, 767 (1997).

[45] X. Sui, T. Hu, J. Wang, B.-L. Gu, W. Duan, and M.-s. Miao, Voltage-controllable colossal magnetocrystalline anisotropy in

single-layer transition metal dichalcogenides, Phys. Rev. B **96**, 041410(R) (2017).

[46] B. Yang, X. Zhang, H. Yang, X. Han, and Y. Yan, Strain controlling transport properties of heterostructure composed of monolayer Cri$_3$, Appl. Phys. Lett. **114**, 192405 (2019).

[47] L. Zhao, T. L. Hung, C. C. Li, Y. Y. Chen, M. K. Wu, R. K. Kremer, M. G. Banks, A. Simon, M. H. Whangbo, C. Lee, J. S. Kim, I. Kim, and K. H. Kim, Cubr2–a new multiferroic material with high critical temperature, Adv. Mater. **24**, 2469 (2012).

[48] C. Wang, D. Yu, X. Liu, R. Chen, X. Du, B. Hu, L. Wang, K. Iida, K. Kamazawa, S. Wakimoto, J. Feng, N. Wang, and Y. Li, Observation of magnetoelastic effects in a quasi-one-dimensional spiral magnet, Phys. Rev. B **96**, 085111 (2017).

[49] M. G. Banks, R. K. Kremer, C. Hoch, A. Simon, B. Ouladdiaf, J.-M. Broto, H. Rakoto, C. Lee, and M.-H. Whangbo, Magnetic ordering in the frustrated Heisenberg chain system cupric chloride CuCl2, Phys. Rev. B **80**, 024404 (2009).

[50] D. J. O'Hara, T. Zhu, A. H. Trout, A. S. Ahmed, Y. K. Luo, C. H. Lee, M. R. Brenner, S. Rajan, J. A. Gupta, D. W. McComb, and R. K. Kawakami, Room temperature intrinsic ferromagnetism in epitaxial manganese selenide films in the monolayer limit, Nano Lett. **18**, 3125 (2018).

[51] M. Herve, B. Dupe, R. Lopes, M. Bottcher, M. D. Martins, T. Balashov, L. Gerhard, J. Sinova, and W. Wulfhekel, Stabilizing spin spirals and isolated skyrmions at low magnetic field exploiting vanishing magnetic anisotropy, Nat. Commun. **9**, 1015 (2018).

[52] A. Fert and P. M. Levy, Role of Anisotropic Exchange Interactions in Determining the Properties of Spin-Glasses, Phys. Rev. Lett. **44**, 1538 (1980).

[53] R. F. Evans, W. J. Fan, P. Chureemart, T. A. Ostler, M. O. Ellis, and R. W. Chantrell, Atomistic spin model simulations of magnetic nanomaterials, J. Phys.: Condens. Matter **26**, 103202 (2014).

[54] X. S. Wang, H. Y. Yuan, and X. R. Wang, A theory on skyrmion size, Commun. Phys. **1**, 31 (2018).

[55] A. Edström, D. Amoroso, S. Picozzi, P. Barone, and M. Stengel, Curved Magnetism in CrI$_3$, Phys. Rev. Lett. **128**, 177202 (2022).

[56] L. M. Sandratskii, Insight into the Dzyaloshinskii-Moriya interaction through first-principles study of chiral magnetic structures, Phys. Rev. B **96**, 024450 (2017).

[57] M. Heide, G. Bihlmayer, and S. Blügel, Describing Dzyaloshinskii–Moriya spirals from first principles, Phys. B (Amsterdam) **404**, 2678 (2009).

[58] G. H. Daalderop, P. J. Kelly, and M. F. Schuurmans, First-principles calculation of the magnetocrystalline anisotropy energy of iron, cobalt, and nickel, Phys. Rev. B **41**, 11919 (1990).

[59] A. Hallal, H. X. Yang, B. Dieny, and M. Chshiev, Anatomy of perpendicular magnetic anisotropy in Fe/MgO magnetic tunnel junctions: First-principles insight, Phys. Rev. B **88**, 184423 (2013).